Electronic Supplementary Information

1 – Instrumentation

NMR experiments were recorded on a Bruker BioSpin 400 MHz NMR spectrometer. Electrospray mass spectra (ESI-MS) were performed using a Thermo Fisher Scientific CTQ Orbitrap XL mass spectrometer. UV-Vis spectroscopy experiments were performed on a Shimadzu UV–-600 spectrophotometer using 10 mm quartz glass cuvettes. IR spectra were collected on a Nicolet Avatar 360 FT–IR spectrometer on KBr disks. Magnetic properties were determined using a Quantum Design MPMS-5XL SQUID magnetometer for direct current (dc) and alternating current (ac) measurements. A microcrystalline sample of **2**–**4** was compacted and immobilised into cylindrical PTFE sample holders. Experimental dc data were recorded at 0.1 T and 1.0 T in the temperature range 2.0–290 K and at 2.0 K in the field range 0.1–5.0 T. Experimental (ac) data were collected at various static bias fields between 0 and 1000 Oe in the temperature range 2.0–50 K and frequency range 3–1000 Hz using an amplitude of $B_{ac} = 3$ G. All data were corrected for the diamagnetic contributions of the sample holder and the complex ($\chi_{m,dia}$ / 10^{-4} cm^3 mol^{-1} = –6.57 (**2**), –6.58 (**3**), –6.60 (**4**)). Single-crystal X-ray diffraction data were collected on a STOE STADIVARI diffractometer with MoKα radiation (**1**), Bruker D8 Venture diffractometer with MoKα radiation (**2** and **4**), and on a Bruker Apex II CCD diffractometer with CuKα radiation (**3**). Powder X-ray diffraction data were recorded with a STADI P (STOE) powder diffractometer.

2 – Analytical characterisation

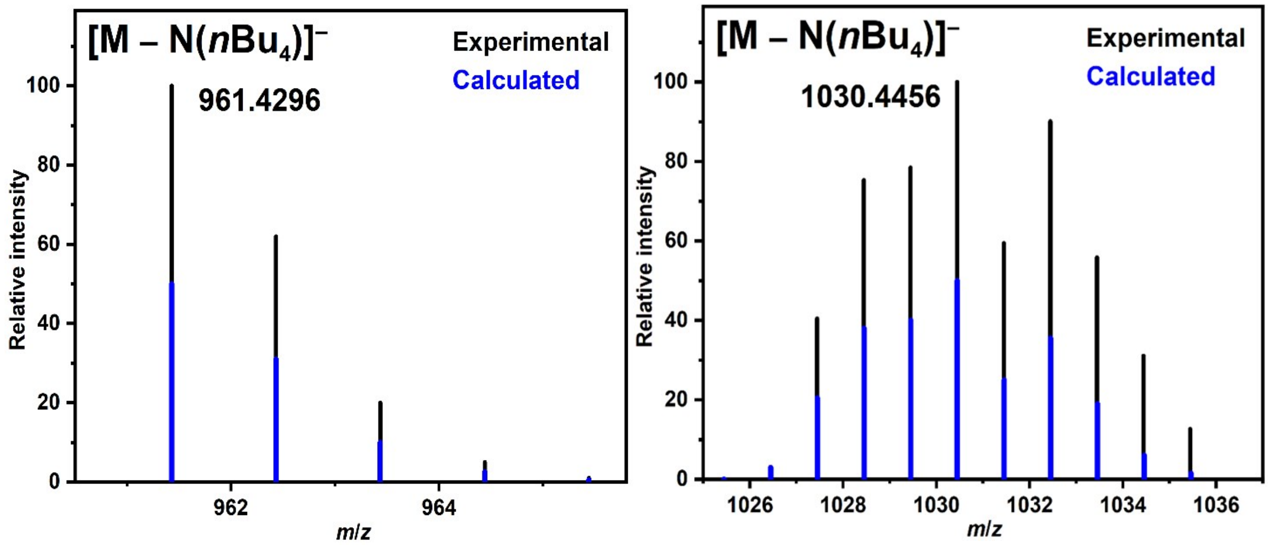

Fig. S1. (**Left**) ESI-HRMS pattern of (N(*n*Bu)$_4$)[Y^{III}L(acac)$_2$] (**1**); *m*/*z*, found 961.42963 [M – N(*n*Bu)$_4$]$^-$ (100%), calculated for [$C_{56}H_{72}O_8Y$]$^-$ 961.4291. M stands for (N(*n*Bu)$_4$)[Y^{III}L(acac)$_2$]. (**Right**) ESI-HRMS pattern of (N(*n*Bu)$_4$)[Gd^{III}L(acac)$_2$] (**2**); *m*/*z*, found 1030.4456 [M – N(*n*Bu)$_4$]$^-$ (100%), calculated for [$C_{56}H_{72}O_8Gd$]$^-$ 1030.4474. M stands for (N(*n*Bu)$_4$)[Gd^{III}L(acac)$_2$]. Calculated relative intensity values have been adjusted to 50% for comparison.

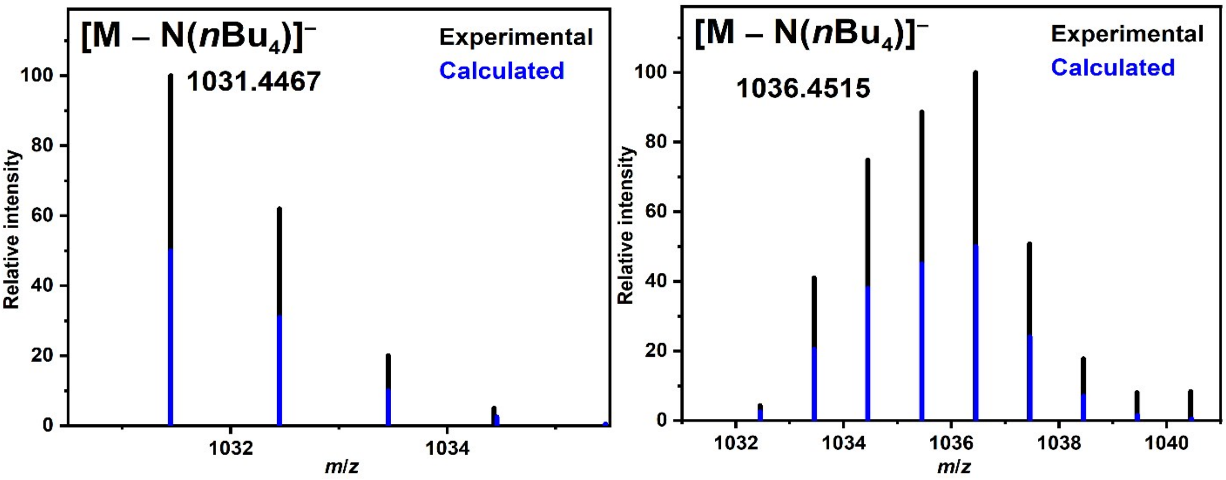

Fig. S2. (**Left**) ESI-HRMS pattern of (N(*n*Bu)$_4$)[Tb^{III}L(acac)$_2$] (**3**); *m*/*z*, found 1031.4467 [M – N(*n*Bu)$_4$]$^-$ (29.86%), calculated for [$C_{56}H_{72}O_8Tb$]$^-$ 1031.4475. M stands for (N(*n*Bu)$_4$)[Tb^{III}L(acac)$_2$]. Calculated and found relative intensity values have been adjusted to 50% and 100%, respectively, for the purpose of comparison. **(Right)** ESI-HRMS pattern of (N(*n*Bu)$_4$)[Dy^{III}L(acac)$_2$] (**4**); *m*/*z*, found 1036.4515 [M – N(*n*Bu)$_4$]$^-$ (100%), calculated for [$C_{56}H_{72}O_8Dy$]$^-$ 1036.4513. M stands for (N(*n*Bu)$_4$)[Dy^{III}L(acac)$_2$]. Calculated relative intensity values have been adjusted to 50% for comparison.

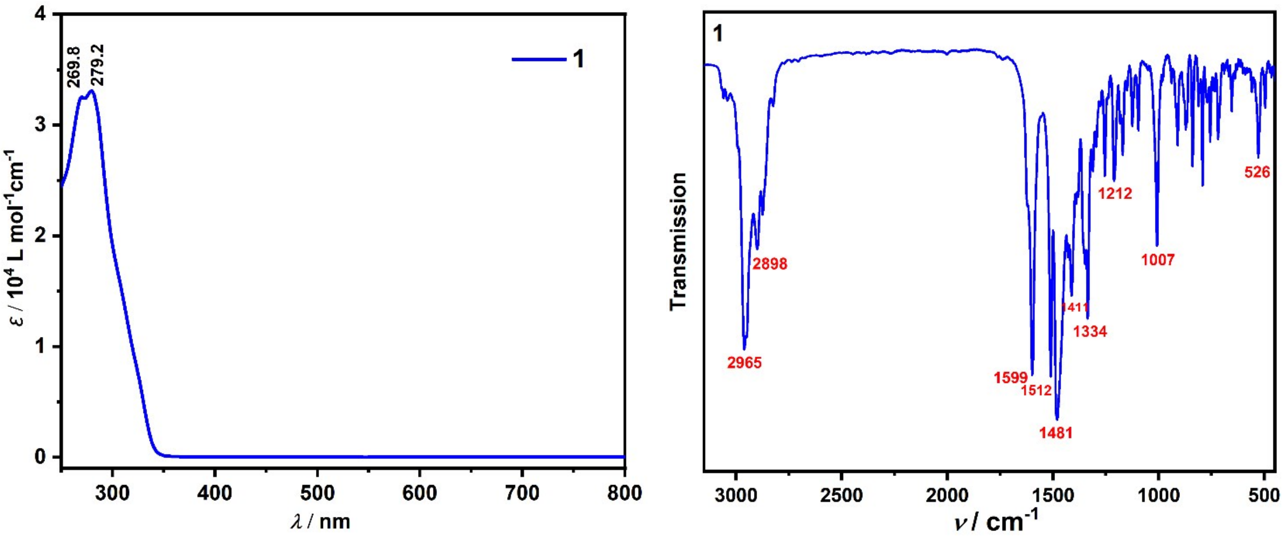

Fig. S3. (**Left**) UV-Vis spectrum of a THF solution of (N(*n*Bu)$_4$)[Y^{III}L(acac)$_2$] (**1**), as representative for the series of **1**–**4**. (**Right**) IR spectrum of (N(*n*Bu)$_4$)[Y^{III}L(acac)$_2$] (**1**) in KBr, as representative for the series **1**–**4**.

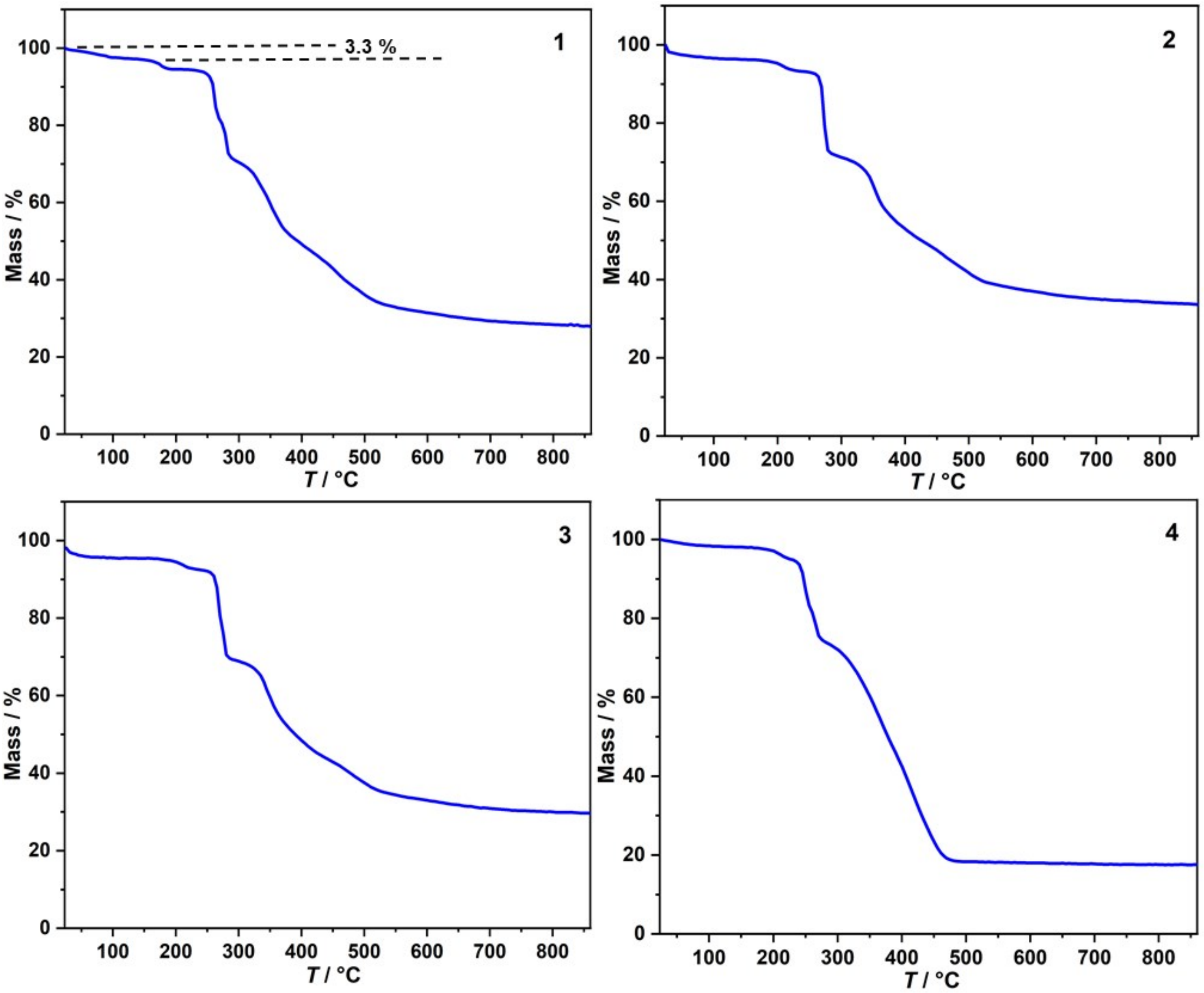

Fig. S4. Thermogravimetric analysis (TGA) for compounds **1**–**4**. Complexes exhibit thermal stability up to ~ 160 °C, related to the gradual loss of CH_3CN crystallisation molecules (3.1–3.3 % of mass loss).

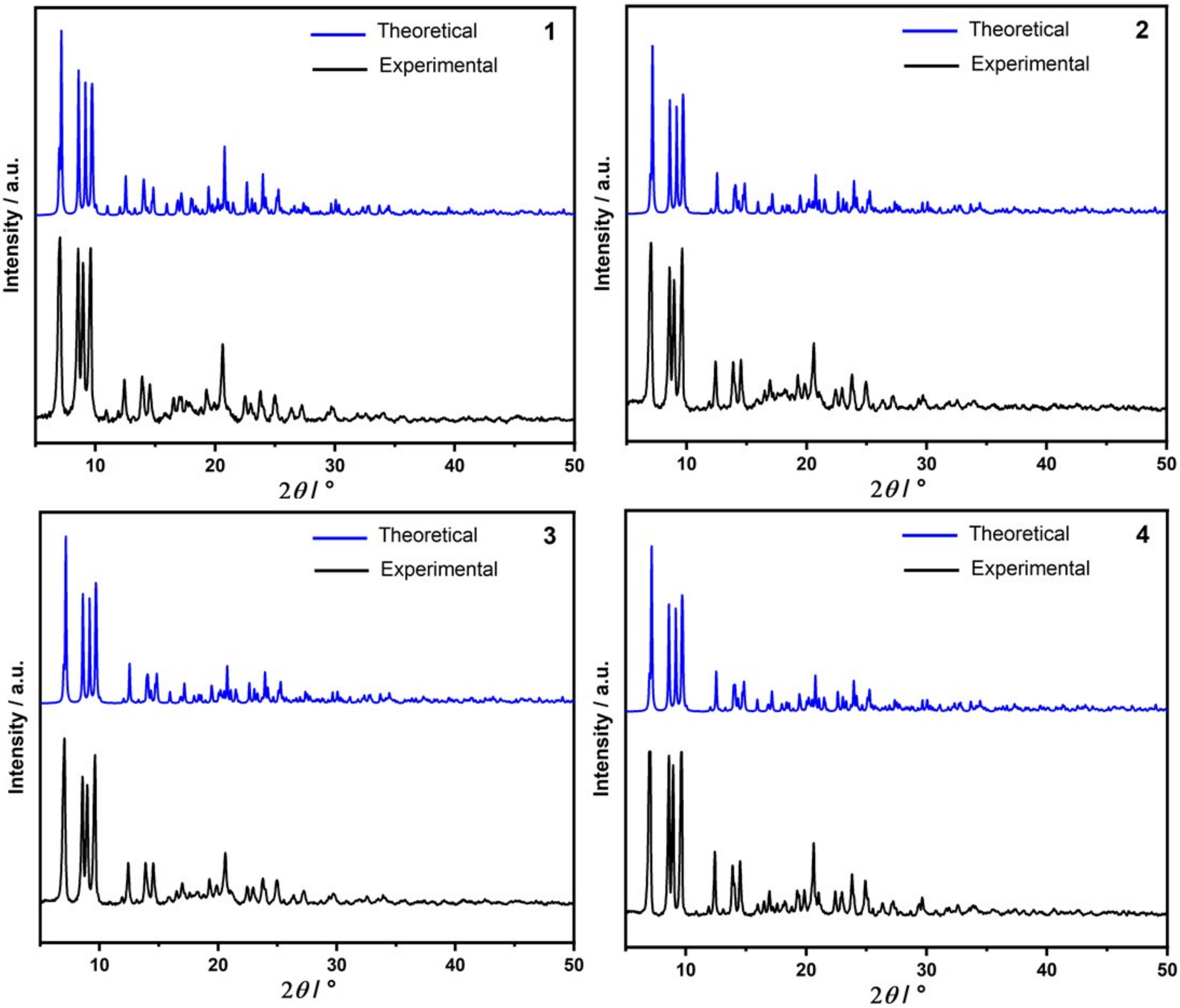

Figure S5. Experimental powder X-ray diffraction (PXRD) patterns measured at RT and theoretical PXRD pattern calculated from single-crystal X–ray diffraction data for compounds **1**–**4**, confirming the homogeneity of the polycrystalline phases.

3 – Crystallographic analysis details

Table S1. Crystallographic data and structure refinement details for **1–4**.

Sample	Gd (**2**)	Tb (**3**)	Dy (**4**)	Y (**1**)
Radiation type	Mo Kα	Cu Kα	Mo Kα	Mo Kα
Empirical formula	$C_{74}H_{111}N_2O_8Gd$	$C_{74}H_{111}N_2O_8Tb$	$C_{74}H_{111}N_2O_8Dy$	$C_{74}H_{111}N_2O_8Y$
M_r / g mol^{-1}	1313.89	1315.56	1319.14	1245.55
Crystal system	Monoclinic	Monoclinic	Monoclinic	Monoclinic
Space group	*C*2/*c*	*C*2/*c*	*Cc*	*Cc*
a / Å	23.8101(7)	23.8191(5)	23.8297(6)	23.819(5)
b / Å	16.0920(5)	16.0761(4)	16.0808(4)	16.065(3)
c / Å	21.0561(10)	21.0672(5)	21.0550(5)	21.035(4)
β	120.3280(10)°	120.3400(10)°	120.3390(10)°	120.37(3)°
Volume / Å^3	6963.6(4)	6962.2(3)	6963.3(3)	6945(3)
Z	4	4	4	4
D_{calc} / g cm^{-3}	1.253	1.255	1.258	1.191
Absorption coefficient / mm^{-1}	1.006	5.412	1.127	0.894
F(000)	2788	2792	2796	2688
Crystal size / mm^3	0.20 × 0.26 × 0.42	0.24 × 0.26 × 0.46	0.20 × 0.26 × 0.40	0.09 × 0.19 × 0.30
Theta range for data collection	2.769° – 25.242°	3.490° – 67.679°	2.770° – 25.242°	2.114° – 25.242°
Completeness to Θ_{max}	99.6 %	99.7 %	99.8 %	99.8 %
Index ranges	$-30 < h < 30$, $-20 < k < 20$, $-27 < l < 26$	$-29 < h < 29$, $-18 < k < 20$, $-26 < l < 25$	$-30 < h < 30$, $-20 < k < 20$, $-26 < l < 26$	$-29 < h < 29$, $-19 < k < 15$, $-25 < l < 25$
Reflections collected	101381	143474	95871	41717
Independent reflections	7678	7092	15176	12916
R_{int}	0.0589	0.0381	0.0177	0.0640
Observed ($I > 2\ \sigma(I)$)	6767	7005	14735	10286
Absorption correction	multi-scan			Gaussian integration
T_{min} / T_{max}	0.6350 / 0.7455	0.5144 / 0.7538	0.6764 / 0.7455	0.7834 / 0.9273
Data / restraints / parameters	7678 / 24 / 470	7092 / 24 / 466	15176 / 2 / 790	12916 / 2 / 767
Goodness-of-fit on F^2	1.363	1.387	1.038	1.036
R_1, wR_2 ($I > 2\sigma(I)$)	$R_1 = 0.0442$, $wR_2 = 0.1093$	$R_1 = 0.0526$, $wR_2 = 0.1398$	$R_1 = 0.0144$, $wR_2 = 0.0388$	$R_1 = 0.0652$, $wR_2 = 0.1588$
R_1, wR_2 (all data)	$R_1 = 0.0516$, $wR_2 = 0.1122$	$R_1 = 0.0529$, $wR_2 = 0.1399$	$R_1 = 0.0152$, $wR_2 = 0.0393$	$R_1 = 0.0876$, $wR_2 = 0.1760$
Largest diff. peak and	0.431 / –0.876	0.468 / –0.771	0.302 / –0.505	0.606 / –1.127

hole / e Å^{-3}				

4 – Magnetic studies

The very small out-of-phase signals of the Gd^{3+} compound **2** in absence of a static magnetic field are shown in Figure S6 (a–c). Since we could observe parts of circles in the Cole-Cole representation of the data, we analysed them in terms of the generalised Debye expression.[1] The found relaxation times τ at each temperature are shown in Fig. S6d and are characterised by a distribution of $\alpha = 0.098 \pm 0.061$, indicating few relaxation pathways. The best reproduction of the data was achieved by the combination of quantum tunnelling of the magnetisation and Orbach relaxation processes, i.e. by the expression $\tau^{-1} = B + \tau_0^{-1}\exp(-U_{\mathrm{eff}}/k_{\mathrm{B}}T)$ that was fitted to the data. The results yield a quantum tunnelling of magnetisation constant $B = (400 \pm 17)\ \mathrm{s}^{-1}$ as well as an attempt time $\tau_0 = (5.35 \pm 0.28)\times10^{-5}$ s and an effective barrier $U_{\mathrm{eff}} = (7.8 \pm 0.2)\ \mathrm{cm}^{-1}$ for the Orbach relaxation process. For the Dy^{3+} compound **4**, the out-of-phase signals observed in the range 1.9 – 2.4 K at zero static bias field cannot be reliably analysed due to the absence of a significant curvature in the Cole-Cole plot. By application of a static bias field of 1000 Oe, very small out-of-phase signals, similar to **2**, are additionally observed (Fig. S7a). We analysed these small signals in terms of the generalised Debye expression (Figures S7a–c) and determined the relaxation times τ shown in Figure S7d. The distribution of the relaxation times α (= 0.363±0.225) points to multiple relaxation pathways, while the τ vs. $1/T$ plot is also in agreement with a single Orbach relaxation process [$\tau^{-1} = \tau_0^{-1}\exp(-U_{\mathrm{eff}}/k_{\mathrm{B}}T)$] within the error margins. This results in an unusually large attempt time τ_0 of $(1.06 \pm 0.16)\times10^{-3}$ s and a small effective barrier $U_{\mathrm{eff}} = (4.0 \pm 0.4)\ \mathrm{cm}^{-1}$. However, since the error margins at $1/T > 0.37\ \mathrm{K}^{-1}$ are very large, we also considered a quantum tunnelling of the magnetisation process and an Orbach relaxation process fitting only the data for $1/T < 0.37\ \mathrm{K}^{-1}$ using $\tau^{-1} = B + \tau_0^{-1}\exp(-U_{\mathrm{eff}}/k_{\mathrm{B}}T)$. This results in a quantum tunnelling of magnetisation constant $B = (110 \pm 8)\ \mathrm{s}^{-1}$, an attempt time $\tau_0 = (2.82 \pm 1.10)\times10^{-4}$ s and, an effective barrier $U_{\mathrm{eff}} = (10.2 \pm 1.4)\ \mathrm{cm}^{-1}$ for the Orbach relaxation process. Since the out-of-phase signals are very weak, we like to stress that the ac susceptibility analysis results for **2** and **4** carry a significant uncertainty.

---

[1] K. S. Cole, R. H. Cole, *J. Chem. Phys.*, 1941, **10**, 98–105.

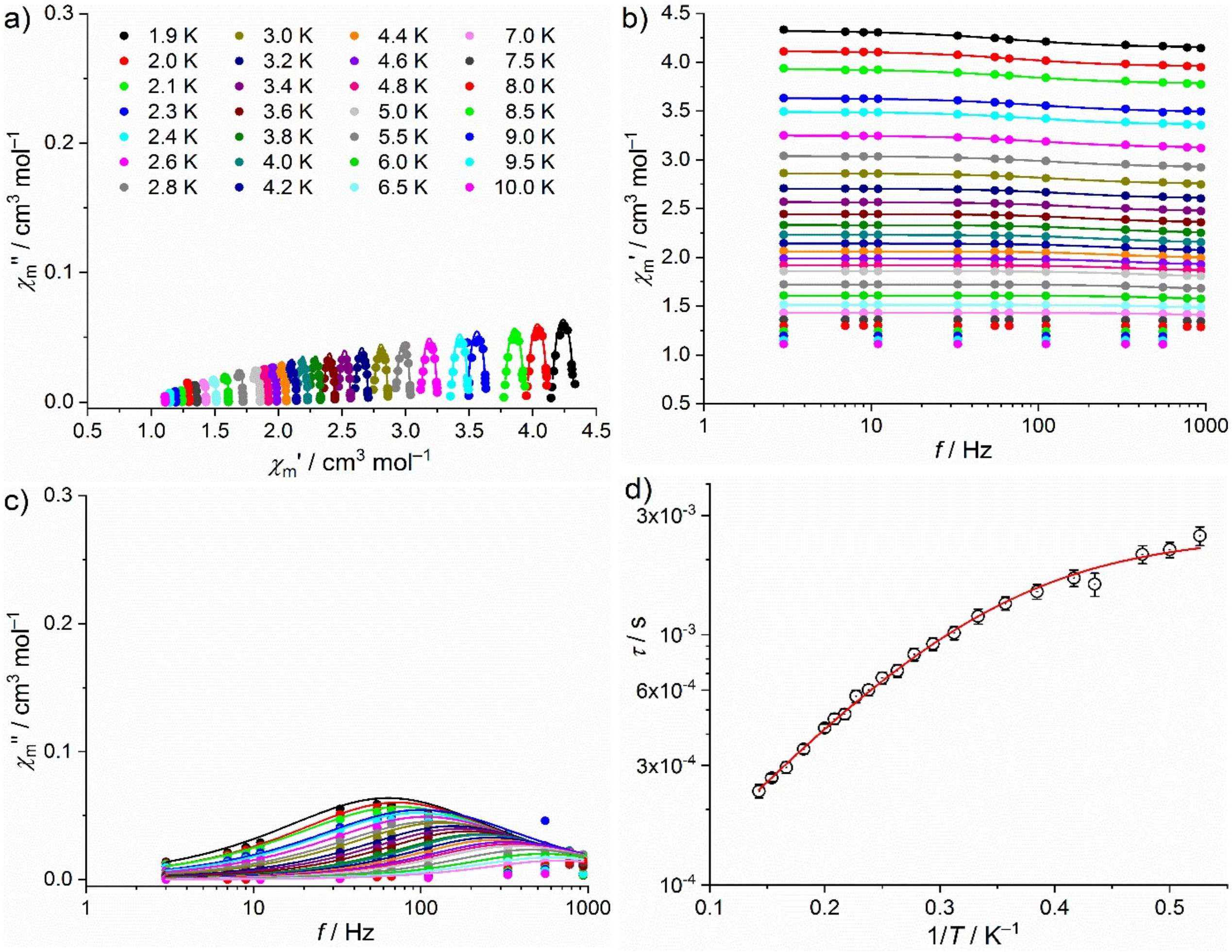

Fig. S6. AC magnetic susceptibility measurements at zero static bias magnetic field for **2**: (a) Cole-Cole plot of in-phase *vs.* out-of-phase susceptibility (χ_m'' *vs.* χ_m'); (b) χ_m' *vs.* applied frequency *f*; (c) χ_m'' *vs.* *f*; (d) relaxation times τ *vs.* reciprocal temperature 1/*T*. Circles represent experimental data. Solid lines: fits to generalised Debye expression (for panels a–c) and fit considering quantum tunnelling of magnetisation and Orbach relaxation processes (for panel d).

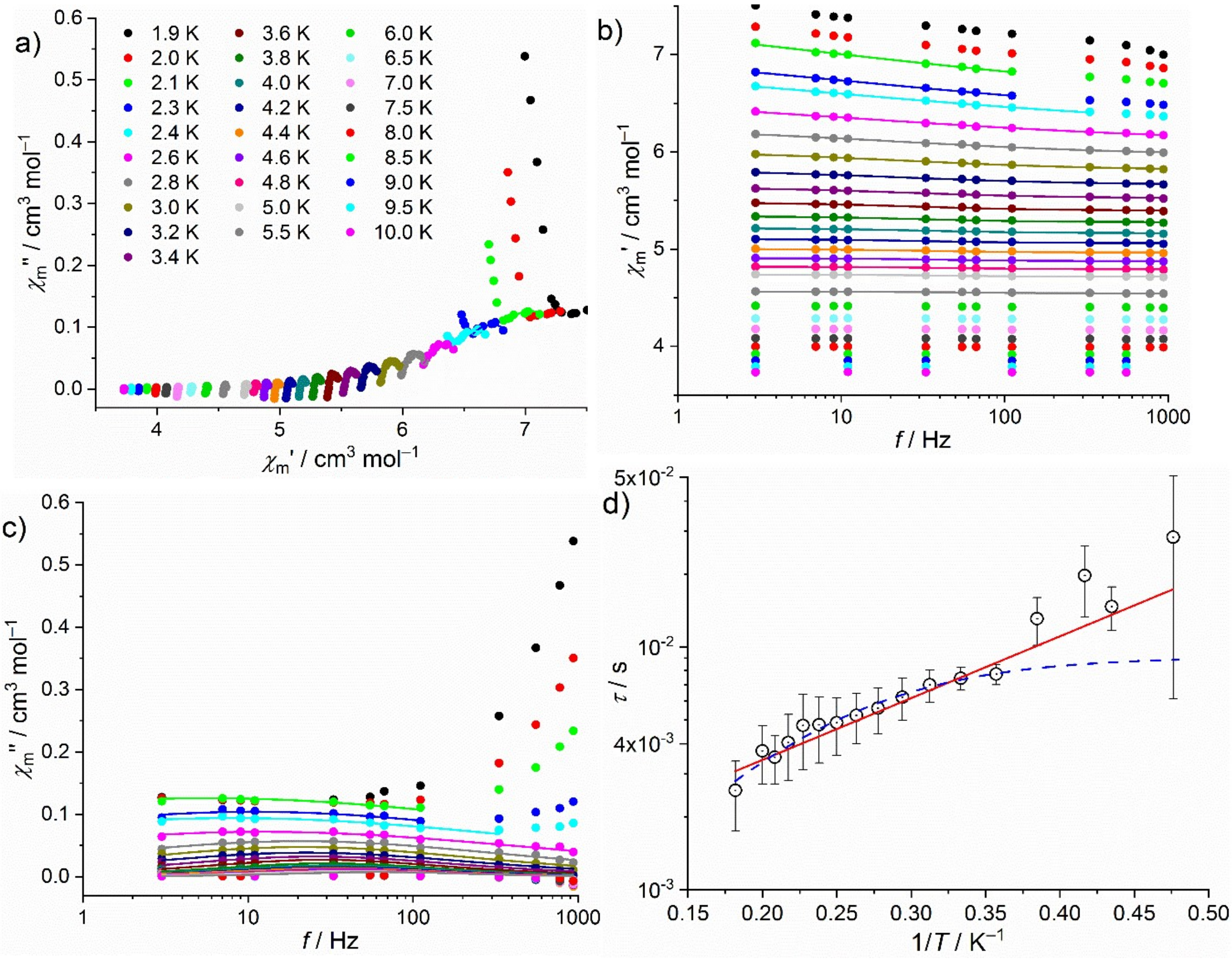

Fig. S7. AC magnetic measurements at a static bias magnetic field of 1000 Oe of **4**: (a) Cole-Cole plot of in-phase *vs.* out-of-phase susceptibility (χ_m'' *vs.* χ_m'); (b) χ_m' *vs.* applied frequency f; (c) χ_m'' *vs.* f; (d) relaxation times τ *vs.* reciprocal temperature $1/T$. Plotted circles represent the experimental data. Solid lines: least-squares fits to generalised Debye expression (for panels a–c) and a fit considering an Orbach slow relaxation process (panel d). Blue dashed line: fit to a quantum tunnelling of magnetisation and an Orbach slow relaxation processes for $1/T < 0.37$ K^{-1} (panel d).

We also fitted the magnetic dc data to extract information about the energetic structure of the lanthanide ions using the computational framework CONDON.[2] The fits account for spin-orbit coupling, interelectronic repulsion as well as the ligand field are shown as solid lines in Fig. S8, and the results regarding the energy states of the ground terms are given in Table S2. The one-electron spin-orbit coupling parameters (ζ_{4f}) and the Slater-Condon parameters (F^2, F^4, F^6) were taken as constants from literature.[3] For the initial ligand field parameters, we extrapolated values using the REC model[4] and assumed local C_{2v} ligand field symmetry. The number of the considered energy microstates corresponds to the number of all electron configurations of the

---

[2] (a) H. Schilder, H. Lueken, *J. Magn. Magn. Mat.* **2004**, *281*, 17–26; (b) M. Speldrich, H. Schilder, H. Lueken, P. Kögerler, *Isr. J. Chem.* **2011**, *51*, 215–227; (c) M. Speldrich, J. van Leusen, P. Kögerler, *J. Comput. Chem.* **2018**, *39*, 2133–2145.

[3] E. U. Condon, G. H. Shortley, *The Theory of Atomic Spectra*, Cambridge University Press, Cambridge, **1970**.

[4] (a) J. J. Baldovi, J. J. Borras-Almenar, J. M. Clemente-Juan, E. Coronado, A. Gaita-Arino, *Dalton Trans.* **2012**, *41*, 13705–13710; (b) J. J. Baldovi, A. Gaita-Arino, E. Coronado, *Dalton Trans.* **2015**, *44*, 12535–12538.

respective 4f^n shell, i.e. 3432 (**2**), 3003 (**3**) and 2002 (**4**). For potential (nearly negligible) intermolecular coupling interactions, we utilise a mean-field approach. The calculated energy states are strongly mixed states as commonly found for lanthanides centres in comparatively low-symmetry ligand field environments.

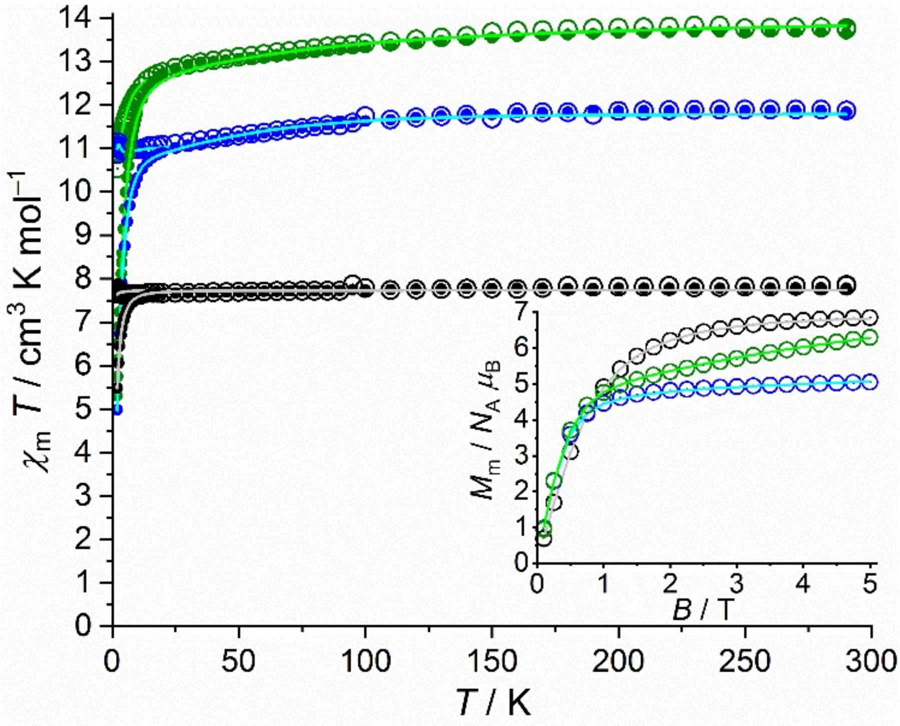

Fig. S8. Fits to magnetic dc susceptibility data: $\chi_m T$ vs. T at 0.1 (empty circles) and 1 T (filled circles) and M_m vs. B at 2.0 K (inset) for **2** (blue circles), **3** (green circles) and **4** (black circles); least-squares fits shown as solid lines with corresponding colours.

Table S2. Energy states (2*J*+1) in cm^{-1} of the ground terms of **2**–**4** (mainly $^8S_{7/2}$ (**2**), $^7F_6$ (**3**) and $^6H_{15/2}$ (**4**) – “next state” denotes the lowest energy state of the first excited term), estimation of intermolecular coupling energies, and quality of the fit (*SQ*, relative root mean squared error). The denotation (s) indicates a singlet and (d) a doublet; the relevant contributions to the wave functions are given in terms of m_J.

energy level	Gd (**2**)	Tb (**3**)	Dy (**4**)
1	0 (d) 57 % |±1/2> + 43 % |∓7/2>	0 (s) 32 % (|+5> + |–5>) + 17 % (|+3> + |–3>) + 1 % (|+1> + |–1>)	0 (d) 22 % |±7/2> + 22 % |±3/2> + 21 % |±15/2> + 11 % |±11/2> + 10 %|∓5/2> + 8 % |∓1/2> + 5 % |∓9/2> + 1 % |∓13/2>
2	0.09 (d) 67 % |∓3/2> + 24 % |±5/2> + 5 %|∓7/2> + 4 % |±1/2>	3.0 (s) 42 % (|+4> + |–4>) + 8 % (|+2> + |–2>)	8.1 (d) 32 % |±9/2> + 30 % |±5/2> + 11 % |±13/2> + 9 % |∓7/2> + 6 %|∓11/2> + 6 % |∓15/2> + 4 % |±1/2> + 2 % |∓3/2>
3	0.11 (d) 52 % |∓7/2> + 39 % |±1/2> + 6 %|∓3/2> + 3 % |±5/2>	12.9 (s) 42 % (|+5> + |–5>) + 8 % (|+3> + |–3>)	16.9 (d) 73 % |∓15/2> + 13 % |∓7/2> + 8 % |∓11/2> + 5 %|∓3/2> + 1 % |±1/2>
4	0.27 (d) 73 % |±5/2> + 27 % |∓3/2>	23.4 (s) 47 % (|+4> + |–4>) + 2 % (|+2> + |–2>) + 1 % (|+6> + |–6>)	166.9 (d) 46 % |±13/2> + 39 % |±1/2> + 10 % |∓11/2> + 2 % |±9/2> + 2 % |±5/2> + 1 % |∓7/2>
5	———	82.2 (s) 32 % (|+3> + |–3>) + 17 % (|+5> + |–5>) + 1 % (|+1> + |–1>)	223.1 (d) 38 % |±3/2> + 28 % |∓1/2> + 16 % |∓5/2> + 8 %|±7/2> + 5 % |∓13/2> + 3 % |∓9/2> + 2 % |±11/2>
6	———	100.5 (s) 35 % (|+3> + |–3>) + 8 % (|+1> + |–1>) + 7 % (|+5> + |–5>)	313.2 (d) 29 % |∓13/2> + 26 % |±11/2> + 19 % |±3/2> + 10 %|∓5/2> + 9 % |∓1/2> + 7 % |∓9/2>
7	———	135.2 (s) 48 % (|+2> + |–2>) + 2 % (|+4> + |–4>)	548.1 (d) 35 % |∓9/2> + 22 % |±11/2> + 16 % |±7/2> + 10 %|∓5/2> + 9 % |∓1/2> + 7 % |∓13/2> +1 % |±3/2>
8	———	150.4 (s) 47 % (|+6> + |–6>) + 4 % |0> + 1 % (|+4> + |–4>)	616.1 (d) 30 % |±7/2> + 22 % |∓5/2> + 17 % |∓9/2> + 14 %|±11/2> + 13 % |±3/2> + 3 % |∓1/2> +1 % |∓13/2>

9	———	153.3 (s) 49 % (|+6> + |–6>) + 1 % (|+4> + |–4>)	———
10	———	165.3 (s) 31 % (|+2> + |–2>) + 26 % |0> + 6 % (|+4> + |–4>)	———
11	———	184.0 (s) 48 % (|+1> + |–1>) + 2 % (|+3> + |–3>)	———
12	———	226.4 (s) 42 % (|+1> + |–1>) + 7 % (|+3> + |–3>) + 1 % (|+5> + |–5>)	———
13	———	231.1 (s) 70 % |0> + 12 % (|+2> + |–2>) + 2 % (|+4> + |–4>) + 1 % (|+6> + |–6>)	———
next state	33081 (d)	1967 (s)	
$-(z2J)$ / cm^{-1}	$(2.1\pm6.3)\times10^{-3}$	–0.56±0.01	–0.24±0.07
SQ / %	0.66	0.59	0.67